Magnetized laboratory plasma jets: Experiment and simulation

Peter Schrafel, Kate Bell, John Greenly, Charles Seyler, and Bruce Kusse

Phys. Rev. E **91**, 013110 — Published 30 January 2015

DOI: 10.1103/PhysRevE.91.013110

Magnetized laboratory plasma jets: experiment and simulation

Peter Schrafel,[*] Kate Bell, John Greenly, Charles Seyler, and Bruce Kusse
Laboratory of Plasma Studies
Cornell University
Ithaca, NY 14853

Experiments involving radial foils on a 1 MA, 100 ns current driver can be used to study the ablation of thin foils and liners, produce extreme conditions relevant to laboratory astrophysics and aid in computational code validation. This research focuses on the initial ablation phase of a 20 µm Al foil (8111 alloy), in a radial configuration, driven by Cornell University's COBRA pulsed power generator. In these experiments ablated surface plasma (ASP) on the top side of the foil and a strongly-collimated axial plasma jet are observed developing midway through the current-rise. With experimental and computational results this work gives a detailed description of the role of the ASP in the formation of the plasma jet with and without an applied axial magnetic field. This ∼1 T field is applied by a Helmholtz-coil pair driven by a slow, 150 µs current pulse and penetrates the load hardware before arrival of the COBRA pulse. Several effects of the applied magnetic field are observed: 1. Without the field XUV emission from the ASP shows considerable azimuthal asymmetry while with the field the ASP develops azimuthal motion that reduces this asymmetry; 2. This azimuthal motion slows the development of the jet when the field is applied; and 3. With the magnetic field the jet becomes less collimated and has a density minimum (hollowing) on the axis. PERSEUS, an XMHD code, has qualitatively and quantitatively reproduced all these experimental observations. The differences between this XMHD and an MHD code without a Hall current and inertial effects are discussed. In addition the PERSEUS results describe effects we were not able to resolve experimentally and suggest a line of future experiments with better diagnostics.

PACS numbers: 52.38.Ph, 52.65.-y, 52.72.+v

---

[*] pcs33@cornell.edu

I. INTRODUCTION

A. Motivation

High energy density physics (HEDP) [1] studies involving exploding radial foils driven by high-current (∼1 MA) pulsed-power machines are of interest for their relevance to: the ablation physics of thin foils and liners, the laboratory study of plasma dynamics comparable to astrophysical phenomena like jets [2], and the validation of new computer codes developed to simulate ever-widening swaths of plasma physics. In this context, a radial foil is a thin (∼10 µm,) metal disk that makes contact with a current source near the center of the foil and is grounded at an outer annulus. Experiments with radial foils have a history along with wire array z-pinches [3], conical wire arrays [4], and radial wire arrays [5].

Recent developments in pulsed-power technology have increased the possibilities for creating laboratory experiments relevant to astrophysical processes. Scaling arguments [6–10] allow us to make reasonable comparisons between lab-scale and astro-scale plasmas if they are sufficiently similar. Extending the parameter space which laboratory experiments can access increases the likelihood that we can produce results of wide interest. Jets are of particular interest because of their astrophysical ubiquity and dynamic properties.

Over the past few decades, the computational capacity for numerical simulations of useful complexity has tremendously increased. Single-fluid magnetohydrodynamics (MHD) models are highly favored for their simplicity and efficiency, although they may leave out important physics in certain situations. Extended MHD (XMHD) codes which retain the Hall term in Ohm's law, as PERSEUS [11] does, allow for the accurate simulation of high-density pulsed power loads such as wires and foils without invoking anomalous vacuum resistivity models. New well-designed experiments are providing valuable information confirming situations where MHD vs. XMHD simulations are valid.

There has been much interest in recent years in experiments involving radial foils for these reasons. Previous investigations on the COBRA [12–16] and MAGPIE [17, 18] pulsed power generators have provided a wealth of compelling results. Newer configurations involve launching the hydrodynamic jet into an ambient medium [19] or modifying the magnetic field of the experiment with a solenoid in series with the load [20]. Imposing the magnetic field with an independent power supply (as we do here) allows for the study of dynamics in an (initially) uniform background field.

This paper presents the results of new experiments and computational simulations of exploding radial foils in the presence of a strong, uniform magnetic field. Section II briefly examines the details of the experimental design. It describes the driver, radial foil load hardware, pulsed coils for applying a magnetic field, and the diagnostics used to collect data. Section III presents the experimental results with an emphasis on the effects of the applied axial magnetic field. Section IV explores the results of computer simulations with parameters chosen to most closely model the experiment. Experiment and simulation come together in Section V, which highlights their strong agreement and explains the major results.

II. EXPERIMENTAL DESIGN

A. COBRA driver

The pulsed-power driver COBRA [21] (COrnell Beam Research Accelerator) nominally provides a current pulse peaking at 1 MA to an inductive load (∼ 10 nH) with a rise time of 100 ns to 200 ns. COBRA has been used for the study of wire array z-pinches and x-pinches, gas puff z-pinches, and several configurations of foil and liner loads. It is a bipartite machine mirrored about its saggital plane. Each half of COBRA is driven by a Marx generator of 16, 1.35 µF capacitors resulting in a total of 106 kJ when the machine is charged to the standard operating voltage of 70 kV. All of the work discussed in this paper involves short pulses on COBRA (rise times of 90 ns to 110 ns reaching peak currents of 0.9 MA to 1.1 MA).

B. Radial Foils

A short and simplified description of the early-time dynamics of an exploding radial foil is helpful to set the coming discussion in context. (See Fig. 1 and its caption for a definition of some important terms like Ablated Surface Plasma (ASP).)

The load hardware (the apparatus used to connect the foil to the COBRA power feed) in these experiments is comprised of a central brass cathode pin and an annular titanium ring that connects the outer radius of the foil to

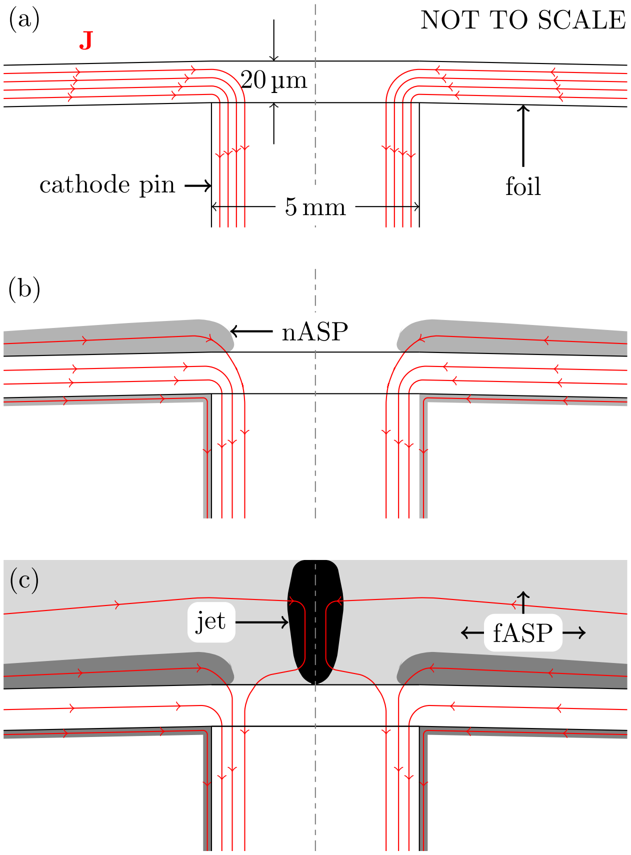

Figure 1. (Color online) A spatially-stretched time-lapse cartoon diagram of a radial foil in the ablation regime. The following times, which indicate time after onset of the COBRA current pulse, are a function of foil and cathode thickness. (a) From 0 ns to 20 ns, the radially inward and axially downward current density **J** driven by COBRA sets up an azimuthal magnetic field **B**. This leads to an upward $\mathbf{J} \times \mathbf{B}$ force along the foil which falls off as r^{-2}. The foil heats up and ablated plasma is pushed upward by the $\mathbf{J} \times \mathbf{B}$ force. (b) and (c) This paper distinguishes between three different locations in the plasma: the *nASP* and *fASP* or *near* (dark gray) and *far* (light gray) ablated surface plasmas respectively, and the central *jet* (black.) The nASP is a relatively high-density region extending up to 1 mm from the surface of the foil, while the fASP is a more diffuse collection of plasma surrounding the entire jet. (b) From 20 ns to 60 ns, the ablated plasma begins to carry some of the current. (c) From 60 ns to ∼200 ns, fASP streaming onto the axis forms the well-collimated jet.

the anode (see Fig. 2). This hardware is similar to that used in previous work with radial foils on COBRA [12–16]. The main difference is that these present experiments all involve thicker 20 µm Al foils (8111 alloy) stretched over a larger 5 mm diameter solid brass cathode. These experimental parameters were empirically chosen to maximize the time in the current pulse before the ‘magnetic bubble’ dominates the plasma dynamics.

C. Helmholtz Coils

This experiment required the development of a system to provide a constant, spatially uniform magnetic field that can be controlled independently of COBRA. A pair of Helmholtz coils (with coil radius equal to the distance between the coils) was designed to be compatible with the COBRA load region and the radial foil hardware. From previous experiments and simulations, the expected azimuthal B_θ due to currents in the jet is no more than a few teslas, so applying a B_z of similar strength would be a significant perturbation and reasonably obtainable for the present investigation. Providing ∼1 T of field to $\sim 10^{-3}\,\mathrm{m}^3$ of space requires ∼1 kJ of energy and electric current ∼100 kA. This current can be split into several concentric turns of a coil. The number of turns can be chosen according to the desired inductance and available materials. The chosen configuration was a pulsed electromagnet with 2 sets of 12 hand-wound turns of Cu-W flat wire potted in an epoxy mold encased in a G10 fiberglass shell. These coils and how they fit around the foil hardware are depicted in Fig. 2.

The rise-time of the coil pulse (∼100 µs) was set to be significantly slower than the rise-time of the COBRA pulse

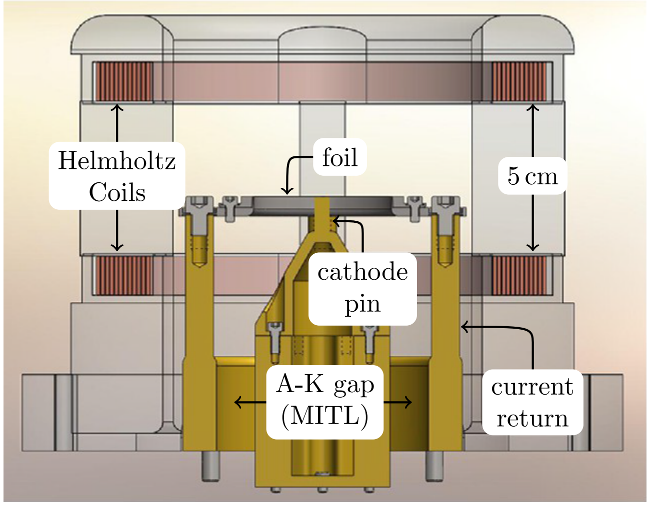

Figure 2. (Color online) A cutaway diagram details the coils for providing an axial magnetic field and the load hardware that connects the radial foil load to the COBRA A-K gap with important parts labelled.

(100 ns) and sufficiently slow to penetrate the foil hardware (minimize azimuthal eddy currents). This ensures the full advantages of the uniform field provided by the Helmholtz coil configuration. But the field should not be able to penetrate the vacuum magnetically-insulated transmission line (MITL) gap and short out that insulation. This is a small concern for this particular set of coils because the radial fringing fields from the Helmholtz coils in the MITL gap are much smaller (by a factor ∼0.01) than the azimuthal MITL fields. The pulser and coils are well approximated as an LC circuit, where L is dominated by the inductance of the coils and C is the capacitance of the energy storage bank. With a 200 µF capacitor bank and ∼50 µH coils, the characteristic timing is $\tau \sim \sqrt{LC} = 100\,\mu\text{s}$. This is not sufficiently slow to fully penetrate the radial foil hardware, so the field strengths quoted in this paper (from $\dot{B}$ measurements made ∼1 mm above the foil) are ∼66% of the 'vacuum' field which is measured in the absense of the foil hardware. Despite the perturbation from eddy currents, the variation in $|B_z|$ in the region of interest above the foil is small (<10%) with the load hardware in place.

The coils can be pulsed in opposite polarities easily by exchanging the feed cables. This allows for switching the orientation (upward or downward) of the applied B_z from one shot to another.

D. Diagnostics

The COBRA vacuum chamber with lines-of-sight of interest is diagrammed in Fig. 3. The main diagnostics of interest for this work are XUV emission pinhole cameras, green-laser-backlit shadowgraphy and interferometry, and spatially-resolved, time-gated optical spectroscopy. Each of these is described in the following sections.

1. *XUV emission*

Two 4-frame pinhole quadrant cameras (QUAD-cams) give spatially and temporally resolved images of the plasma where it is warm and dense enough to emit light collected through 200 µm pinholes and detected by the multi-channel plate (MCP.) The MCPs are triggered to provide ∼1 ns-long exposures separated by 10 ns. In these experiments one of the QUAD-cams (QC1) looks along the axis at emission from the hot plasma above the foil (skip ahead to Fig. 5 to see this). QC1 captures images of the thermal instability of the nASP. The other QUAD-cam (QC2) sees the plasma development side-on and clearly shows the profile and development of the axial jet (skip ahead to Fig. 6).

2. *Interferometry*

A 120 ps, 532 nm (frequency-doubled ND-YAG) EKSPLA laser provides light for spatially and temporally resolved backlighting and interferometry. Before entering the experimental chamber it splits into three separate paths of

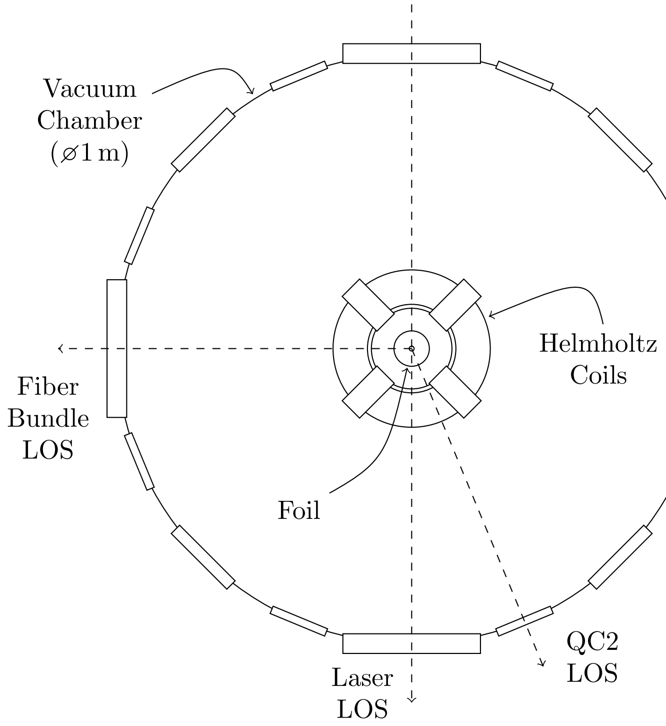

Figure 3. An axial view of the COBRA load and diagnostics shows lines-of-sight for the main diagnostics. QC1's viewpoint is the same as the figure perspective, magnified to just see the full extent of the foil. QC1 and QC2 are XUV-emission diagnostics. The laser LOS involves backlighting and interferometry. The fiber bundle collects light for the spectroscopic diagnostic.

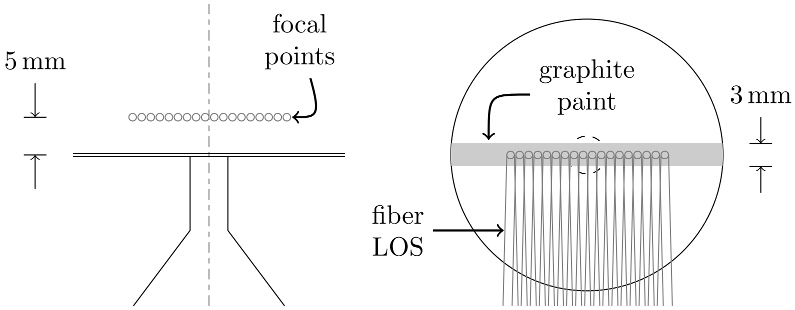

Figure 4. This cartoon explains the carbon seeding for the spectroscopic diagnostic, showing the location of the graphite paint and the positions of the fiber bundle focal points and lines-of-sight.

distinct lengths allowing us to probe the experiment at three times separated by ∼10 ns. These three beams enter the COBRA chamber at a very small ($< 5°$) angle with respect to one another and intersect at the load. They are collected by separate sets of focussing optics including a compound lens and recorded with DSLR CCD cameras. Beam splitting and recombination for interferometry is accomplished between the focussing optics and camera with an air-wedge shearing interferometer [22].

3. *Visible Spectroscopy*

After an early experiment showed evidence of an azimuthal velocity induced by the applied B_z, it was decided to implement a spectroscopic diagnostic to look for a Doppler shift in emission lines in the ASP around the jet. This work uses an ultra-fast gated Gen 3 ICCD camera from Andor (model DH340T-18U-63) coupled with an Andor SR750 Czerny-Turner spectrometer that has a focal length of 750 mm, with a 2400 lines per mm grating blazed for 400 nm. With a custom lens for spectroscopic imaging, this setup allows for a spectral resolution better than 0.4 Å. An 18-fiber bundle collects light from focal points spread across the radius of the foil, 5 mm above the foil. To provide enough light for analysis, spectra are integrated over 40 ns near the peak of the current pulse. Although Al spectral lines were too weak to make conclusive measurements, a C-III doublet was visible which was further enhanced by seeding the foil with carbon. A 3 mm-wide stripe of graphite (Aerodag-G) was painted on the foil perpendicular to the line of sight of the light-collecting fiber bundle. This arrangement is diagrammed in Fig. 4. The thin graphite stripe was used because having excess carbon (painting the whole foil) ablated into the fiber lines-of-sight made subtle Doppler shifts unobservable. Experiments verified that the carbon does not move far from its seeding position over the integration time. When this small quantity of graphite ablates, it significantly increases the population of C atoms in the plasma without having a noticable effect on the overall plasma dynamics as observed with the interferometry and XUV-emission diagnostics. The additional carbon gives a much stronger signal that can be analyzed to find the Doppler shift due to the rotation of the jet. Because of the high collisionality of the ASP ($\nu_i > 10^9\,\mathrm{s}^{-1}$) relative to our timescale of interest, is it reasonable to say that the carbon tracer atoms move in the same sense as the aluminum plasma. Their effect on the magnitude of that motion is not addressed in this work.

III. EXPERIMENTAL RESULTS

A. Electrothermal Instability

In the early stages of metal foil or liner ablation, small perturbations in density result in different regions of plasma having different conductivities. If the plasma is in a regime where conductivity increases with rising temperatures, this positive feedback leads to the development of discrete paths or filamentation of enhanced current flow. These asymmetric current channels can seed the development of dynamically larger-scale instabilities like the magneto-Rayleigh-Taylor instability (MRT) [23]. Understanding the origins and development of these instabilities can lead to better methods for mitigating their undesirable effects.

This plasma electrothermal instability may be present in our experiment. Early in the current pulse, some of the current begins to flow in the nASP above the radial foil surface. XUV emission from this plasma was observed by QC1 looking from above at the top of the foil (see Figure 3). Three sequences of these images are shown in Figure 5 for three different applied magnetic field conditions, $B_z = 0\,\mathrm{T}$, 0.25 T and 1.0 T. These images were taken at 10 ns intervals starting approximately at current peak (100 ns). Several things can be seen in these images. The transition from more intense to less intense emission appears to be consistent with the boil radius, where sufficient ohmic energy has been deposited into the metallic foil to vaporize the entire thickness. This radius increases in time consistent with the radial dependence of the current density. This effect was seen for all magnetic field conditions. For the case of no applied magnetic field it can be seen that the nASP current appears to flow in several (~ 20) discrete paths (tendrils) established by a plasma electrothermal instability. These tendrils expand radially and persist for long timescales (∼100 ns). They appear to interact with several close pairs merging over time. This supports the idea that the tendrils are channels of conductive plasma that carry some of the current. Our interpretation is that the plasma electrothermal instability is responsible for the original formation of the tendrils and a pinching force plays a role in their merging.

A series of exploratory experiments was performed using permanent magnets to apply a modest $B_z \sim 0.1\,\mathrm{T}$ to see the effects on the current structure in the nASP [24]. These experiments showed that the flow direction and development of the tendrils was modified by the $J_r \times B_z$ force density and that they took on a spiral or pinwheel appearance. In order to study these effects more completely the Helmholtz coil shown in Figure 2 was constructed to apply a relatively uniform $B_z \leq 1\,\mathrm{T}$. With a $B_z = 0.25\,\mathrm{T}$ the outer tendrils have wrapped around to result in an azimuthally continuous XUV emission. Some azimuthal variation of the tendrils remains within the melt circle. This condition is shown in the middle series of images in Figure 5. With the strongest magnetic field, $B_z = 1.0\,\mathrm{T}$ there is essentially no indication of the tendrils as shown in the lower series of images in Figure 5.

Another interesting feature is in the XUV emission that occurs near the center of the foil. Near the center of the foil, early in time, there is a region of very little XUV emission. This corresponds to the radius of the hollow cathode pin. During this time the current in the foil is diverted down the cathode pin. This region of lower emission persists until the jet is formed and the emission right on the axis is filled in. This occurs for all the three magnetic field cases shown in Figure 5 with the only difference being that with stronger applied Bz the jet is formed later in time.

B. Jet Dynamics

About 125 ns after the onset of the current pulse, the ablated plasma forms the jet. There are two significant changes to the development of the jet due to the applied B_z. First, the jet appears later in time. This can be clearly seen in side-on XUV emission imaging. Figure 6 gives a comparison. There is a ∼20 ns delay between the

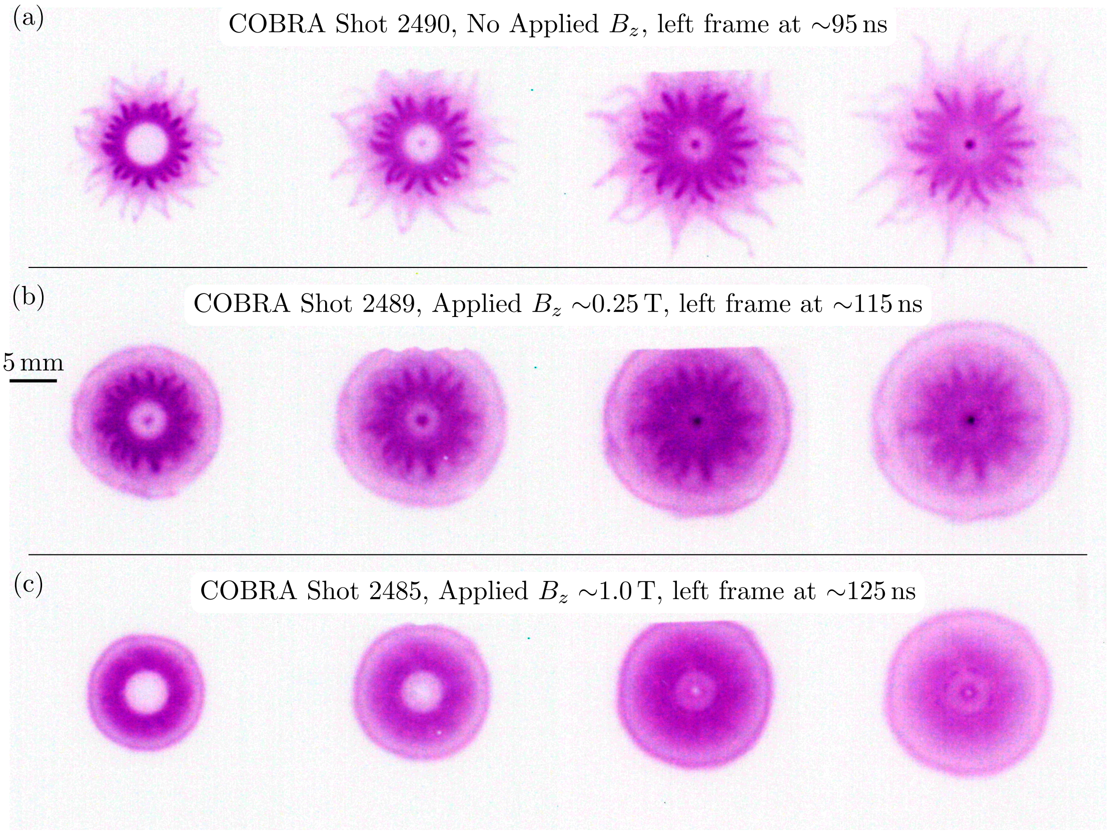

Figure 5. (Color online) Three sets of axial (QC1) views of exploding radial foils on COBRA clearly show the effect of imposing B_z with the Helmholtz coils. In each set of images, there is 10 ns between frames with the earliest on the left. Quoted times are relative to the onset of the current pulse. The tops of the 2nd and 3rd frames of each set are masked by the edge of the detector. The same linear scale applies to each set of images. (a) With no applied B_z, the current-carrying plasma tendrils described in section III A are visible. At an inner radius there is a region of enhanced emission with a more 'regular' azimuthal variation. Further in, there is a disk of very little emission early in time which corresponds to the area of the cathode pin. Because of the small skin depth of the brass pin, minimal current passes through the center of the foil, so it doesn't heat up significantly. Later in time, warm plasma accumulates in this central region, forming the distinct and well-collimated jet. The jet appears only as a dot in the axial view because of the perspective. (b) With a small (0.25 T) applied B_z, the outer tendrils have wrapped around each other to become an indistinct blob. Some azimuthal variation remains within the 'boil circle' defined in section III A. The jet appears similarly to the one in (a). (c) With a strong (1 T) applied B_z, there is practically no azimuthal asymmetry. The jet forms later in time and does not fill in the axis, instead resembling a donut from this perspective.

first appearance of the jet in the case without the applied B_z versus the case with. Second, the jet that forms in the presence of the applied B_z ∼1 T is significantly hollowed on-axis. There is a drop in electron density near $r = 0$ along the axial extent of the jet. Along with this hollowing, the jet takes on an angular 'V' or conical shape as opposed to the more straight-edged cylinder it forms as in the absence of an applied B_z. Figure 7 shows these effects in laser back-lit interferometry.

C. Azimuthal Velocity

The experimental search for an azimuthal velocity in the ASP developed from our observations of the 'washing-out' of the tendrils with the applied B_z. An initial investigation involved a thin, tall 'fin' of mylar extending from $r = 0$ to the outer edge of the foil. With the mylar fin in place, COBRA shots were run with upwards and downwards applied B_z and we observed enhanced XUV emission along different sides of the mylar fin. In each case, the side with enhanced emission corresponded to the side impacted by $J_r \times B_z$ rotation of the nASP. The spectroscopic diagnostic showed distinct C lines in the plasma near the mylar, and motivated implementation of the carbon seeding experiment described in section II D 3. The enhanced lines show an unambiguous shift in wavelength for the focal points farther from the jet. Figure 8 summarizes this result.

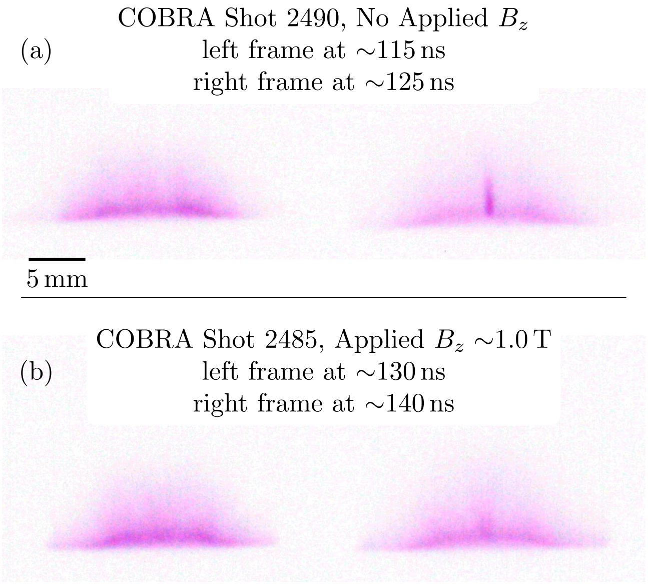

Figure 6. (Color online) Side-on XUV emission imaging (QC2) shows the initial formation of the jet shortly after peak current on COBRA. The same linear scale applies to each set of images. (a) There is a distinct transition between these frames (spaced 10 ns apart) in which the jet becomes apparent. (b) In the case with the applied field, the formation of the jet is delayed by ~15 ns.

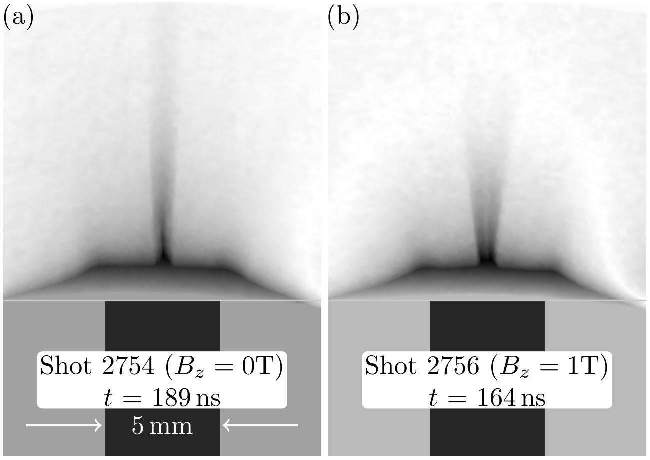

Figure 7. Side-on laser-backlit interferometry was processed to give this comparison of line-of-sight integrated phase shift ($\propto$ areal electron number density). Numerical Abel inversion gives volumetric densities approaching $10^{26}\,\mathrm{m}^{-3}$. The same linear scale applies to each image. (a) The no-field case shows the hydrodynamic jet familiar from previous radial foil work. (b) Adding B_z hollows the jet on axis and widens the angle of its divergence.

D. Physical Picture

These results allow a qualitative physical picture of the development of the ASP and the role it plays in the generation of the plasma jet. The experiment starts with the foil at room temperature (300 K), surrounded by a $\sim 10^{18}\,\mathrm{m}^{-3}$ vacuum. Current begins to flow radially inward toward the center of the foil and then downward in the cathode pin to set up an azimuthal B_θ resulting in an upward force on the radial current (See Fig. 1[a]). As the COBRA current ramps up the foil warms up due to Joule heating. The skin depth of the COBRA pulse in the 20 µm Al foil is ~40 µm and as the foil heats up the cooler regions are less resistive and draw more current [25] with the result that the foil is very uniformly heated azimuthally and in cross-section. Once the foil material has melted, vaporization begins to occur and ablated plasma is observed in the plasma above the foil in XUV imaging. This ASP above the foil is accelerated upward by the $\mathbf{J} \times \mathbf{B}$ force with this force increasing inversely with radius. There is likely ablated

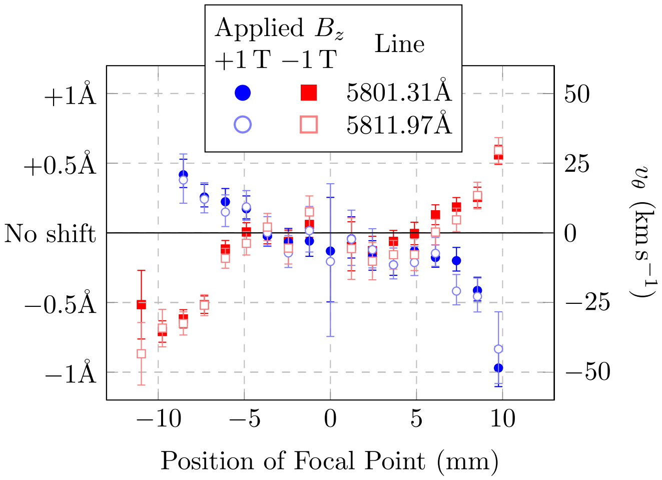

Figure 8. (Color online) Processed spectra from two COBRA shots (2822 & 2823) with graphite painted on the foil to accentuate a C-IV doublet (lines at 580 nm & 581 nm) indicate a lineshift in the outer edges of the ASP for focal points >5 mm away from the axis. If this lineshift is interpreted as a Doppler shift, the outer ASP rotates at speeds $\sim$50 km s^{-1}, as indicated on the right axis. The direction of the shift is consistent with the direction expected from $\mathbf{J} \times \mathbf{B}$ forces. The jet is nearly the same size as the focal points and it emits relatively bright continuum radiation, so it cannot be effectively probed with this diagnostic.

plasma on the underside of the foil but it cannot be directly observed because of the load hardware (See Fig. 1[b]). The ASP below the foil will be accelerated into the more dense foil material. The current in the rising ASP above the foil must connect to the cathode pin and a vertical current channel and azimuthal B_θ is generated in the ASP just above the cathode pin. This B_θ gives the ASP an inward momentum. The stagnation of these radially inward and upward flows leads to the formation of the jet with upward fluid momentum and a downward current (See Fig. 1[c]). The jet is collimated by the pinching action of the downward current and the B_θ field. When a vertical B_z magnetic field is applied two basic things happen: azimuthal velocities are generated in the ASP and the colimation of the jet is reduced by the trapped B_z field lines. After the time scales of this investigation the foil material around the cathode pin is pushed further upward forming a magnetic bubble and a stagnated z-pinch is formed above cathode pin.

IV. SIMULATION

The PERSEUS XMHD code has been developed at Cornell for the study of z-pinch plasma physics, exploding wires and foils and laboratory astrophysics. Its initial goal was the proper treatment of the plasma-vacuum interface [26] by means of electron inertia terms and lower density plasma dynamics by including a Hall term in a generalized Ohms law.

These simulations have been very successful in reproducing our experimental observations both qualitatively and quantitatively. There has been no need to impose an anomalous resistivity to handle the plasma-vacuum interface. In addition to helping to interpret the physics of the experimental observations the code results have described effects that we were not able to observe because of the resolution of our diagnostics and that will be the subject of further study.

The two-dimensional XMHD simulations presented in this paper use cylindrical symmetry (r-z), which imposes azimuthal uniformity on the results. This is clearly nonphysical, considering the significant asymmetries seen in the experiment (see Fig. 5). 3D PERSEUS simulations have not been run at sufficient resolution to explore the formation of the tendrils. For this present investigation, the 2D simulations capture meaningful results that clearly match the experiment. The work presented in this paper has a 500 × 500 cell simulation grid running along $0 < r < 18$ mm and -4 mm $< z < 15$ mm. The results have been mirrored about the z-axis to provide symmetrical images for comparison to the experiment.

It should be pointed out that we also ran standard MHD simulations that required the anomalous resistivity to handle the plasma-vacuum interface to see if the Hall term of XMHD was important. We found that the standard MHD solutions also gave good qualitative and quantitative results (See Fig. 10). However, we have studied laboratory plasma jets produced with opposite pulsed power polarity. In this opposite polarity situation the Hall term of XMHD results in dramatic effects on the rotation and hollowness of the jet that have been observed in some initial laboratory experiments but are not present in MHD simulations. These effects were described in one of the referenced papers

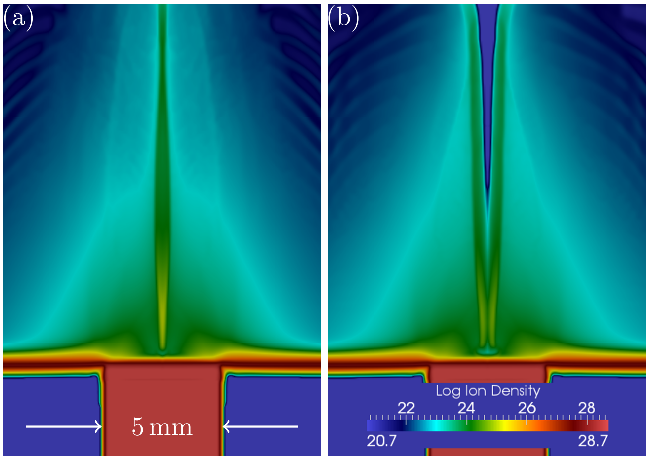

Figure 9. (Color online) A PERSEUS simulation of an exploding radial foil is pictured as a log-plot of ion number density. The same linear scale applies to each image. (a) The no-field case shows a narrow jet with a small angular divergence. The jet's density does not significantly dip on axis. (b) With a 1 T B_z, the jet is wider, more divergent, and has a distinct axial hollowing.

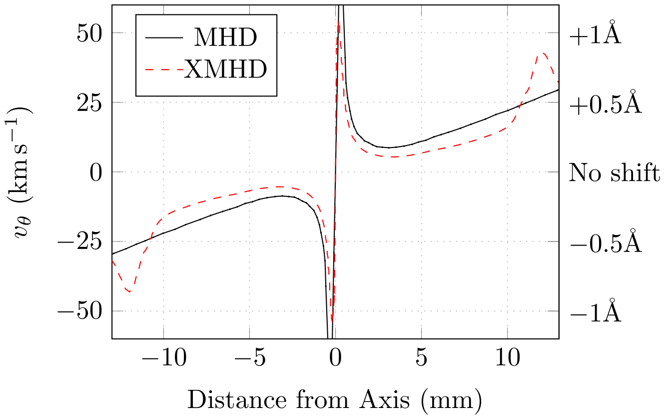

Figure 10. (Color online) Because of the implicit azimuthal symmetry in the $r - z$ simulation, the azimuthal fluid velocity v_θ is everywhere zero in the absence of an applied B_z. With a 1 T B_z, a line-out of $v_\theta(r)$ for z =5 mm looks like this. It shows high speeds in the jet where present diagnostics cannot probe spectroscopically. The speeds in the ASP increase with radius, a behavior which agrees with the line-shifts seen in the experiment. Equivalent Doppler shifts are given on the right axis for comparison to the experiment.

[16] and are the subject of continued study in our laboratory.

A. Density Results

The first goal of the simulation work is to make as direct comparisons to the experiment as possible. Interferometric measurements of electron density can be compared to simulation results of ion density (depicted in Fig. 9). The behavior of the simulation with the applied B_z qualitatively agrees with the experiment. To make direct numerical comparisons, an average ionization rate must be assumed. These simulations used $Z = 3$, which is appropriate for the average expected temperatures in the region of interest ($\sim 50\,\mathrm{eV}$).

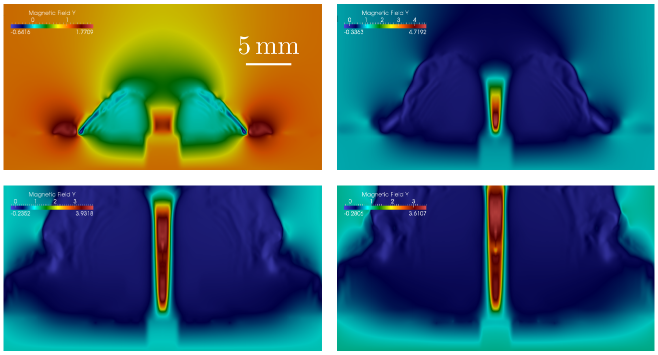

Figure 11. (Color online) Four frames of B_z from a PERSEUS simulation with an initial imposed 1 T field show the strong compression of B_z into a funnel on axis. The same linear scale applies to each image. These images are ordered in time in a 'Z' shape, starting in the top left quadrant. The peak fields on axis approach 4 T.

B. Azimuthal Velocity

The Doppler shift indicated by the spectroscopic diagnostic provides experimental evidence of an azimuthal velocity in the ASP. Figure 10 shows v_θ from the simulation with B_z. Ignoring the jet itself, the general trend of increasing velocity far from the jet matches the experiment. The high velocities near the jet seen in the simulation are interesting because they hint to azimuthal currents which may be responsible for the change in jet behavior via B_z compression.

C. Magnetic field compression

A secondary goal of the simulation work is to search for physical explanations for dynamics using parameters not easily accessible in the experiment. It is difficult to do in-situ probing of magnetic fields without perturbing the plasma significantly. The simulation results show a compression of the applied magnetic field onto the axis (see Fig. 11) that is likely responsible for the modified behavior of the jet. In the simulations the initial B_z gets enhanced on axis by a factor ~ 4. This magnetic compession is supported by currents on the surface of the jet consistent with the large v_θ near the jet as shown in Fig. 10.

V. ANALYSIS

This section outlines the analysis methods used to process raw data collected in this investigation and then summarizes the major findings.

A. Interferometry

Interferograms captured in this dataset had a high fringe density of $4\,\mathrm{cm}^{-1}$ in the unperturbed case. Raw images from the experiment were digitally expanded (magnified) and the fringes were manually traced onto a binary (black and white) layer. This eliminated the possibility for any ambiguity or error introduced by FFT-related interferogram smoothing and denoising algorithms. A simple counting script was run on the binary fringe layer to number each fringe. Cells between fringes were then linearly interpolated along lines running perpendicular to the unpeturbed fring orientation. This was used as an input to a variation-minimizing Gauss-Seidel relaxation routine, which smoothed the dataset but kept the fringe-count value on each fringe constant.

The areal electron density was converted to volumetric electron density with a simple numerical method based on the inverse Abel transform integral.

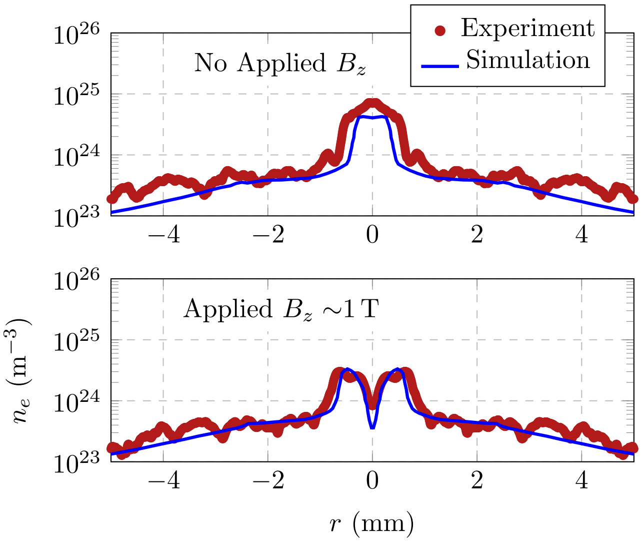

Figure 12. (Color online) Figure showing comparison of density from experiment and simulation. $3n_i = n_e$ (thin blue line) from the PERSEUS simulation is plotted on top of n_e (overlapping red dots) Abel inverted from interferograms.

B. Spectroscopy

As described, rotation of the nASP was observed by Doppler shifts in its visible emission collected by the fiber optic bundle. Shortly before each COBRA shot, the alignment of the fiber bundle image was observed with a Ne lamp placed by the collection optics to ensure that spectra from different fibers did not overlap. These spectra were saved to provide a known-wavelength calibration for the different parts of the image on the ICCD. Then the shot data could be recorded. For analysis, the Ne lines were fitted to a Gaussian profile (due to the spectrometer) which gave spectral resolution for each fiber and each wavelength. This calibration was applied to the shot spectrum of each fiber individually. To find the line positions, Lorentzian profiles (the shape is dominated by Stark broadening) as well as a flat continuum background (reasonable because of the high resolution and small bandwidth) were fitted to these lines. The experimental results have been shown in Fig. 8 and compare qualitatively and quantitatively with the simulation results shown in Fig. 10.

C. Experiment vs. Simulation

The PERSEUS XMHD code was used for our simulations. This code had electron inertial terms and a Hall term in a generalized Ohm's Law, which are not include in a standard MHD code. Figures 6-12 show the outstanding qualitative and quantitative agreement between the experimental and simulation result. Caution is needed for the direct quantitative comparison shown in Fig. 12 because the experimental data shown was taken from interferograms 189 ns and 164 ns into the current pulse, while the simulation result is from 120 ns into the current pulse. No other scaling or normalization was performed. In all cases the PERSEUS XMHD code does not require an anomalous resistivity to handle the vacuum-plasma interface.

As has been pointed out, for the parameters of the experiments discussed in this paper there was not a significant difference between MHD and XMHD simulation results. They boh gave good agreement with the experimental observations. However in reversed pulse power polarity the XMHD and MHD simulations give drastically different results with the XMHD solutions in much better agreement with some initial experiments performed in this reversed polarity [16]. Jets produced in this reverse polarity are the subject of our current and future work.

D. Conclusions

This work has explored the early ablation regime of an exploding radial foil under the influence of a strong, uniform axial magnetic field. It shows that the addition of the field reduces assymetries due to an electrothermal instability in the current-carrying ablated plasma. The field also affects the central plasma jet, which becomes wider, more

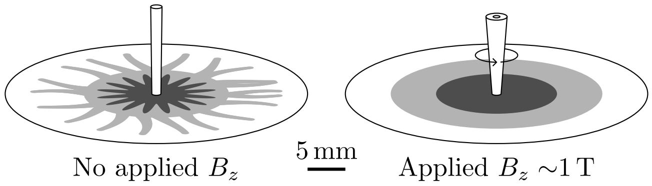

Figure 13. Cartoon of the jet formed by an exploding radial foil illustrating the major findings of this investigation. The jet becomes a hollow cone as it compresses the applied B_z on axis, azimuthal assymetries in the nASP become indistinct due to the azimuthal motion of current-carrying plasma. The fASP (not pictured) also takes on the same sense of rotation as the jet.

divergent, and hollowed on-axis with the applied field. A Doppler shift seen with optical spectroscopy confirms the hypothesis of significant fluid rotation in the plasma surrounding the jet. These results are summarized in Fig. 13. XMHD computational simulations provide results in striking agreement with the experiment with regards to jet formation, dynamics, and the plasma rotation. Simulations demonstrate that a probable cause for the hollowing of the jet is a compression of the applied B_z onto the axis due to the inward flow of the ablated plasma.

Magnetic field compression is compatible with the observations of the changes in jet dynamics. The magnetized jet is hollow because the magnetic pressure of the compressed B_z excludes the ASP from reaching the axis to form the jet. The jet is conical because the exponentially higher densities closer to the foil lead to higher kinetic pressure (the temperature variation is probably not as strong), allowing more compression of the B_z. As this density falls off with distance from the foil, the edge of the jet moves out radially. The jet develops later in time with the applied B_z because the azimuthal velocity increases the effective distance that plasma must travel to converge on axis.

E. Future Work

As mentioned, future work will include a series of experiments that operate the radial foil plasma jet generation in opposite polarity. Under these conditions the simulations have shown a marked difference between the MHD and XMHD results with the XMHD results in much better agreement with some initial experiments. This clearly merits further investigation.

There are some features of the simulation results that we were not able to confirm experimentally and are important for further study because they have implications for the physics of how these laboratory plasma jets are formed. One is the magnetic compression indicated in Fig. 11. Attempts to use small $\dot{B}$-loop probes placed above the jet proved inconclusive because a shock front was observed forming against the probe. Measurements outside of the jet or further above the jet will be tried to look at the fringing field effects of the compression. Faraday rotation will also be attempted. Another feature of the simulations that may be connected with the magnetic compression is the sharp increase in the rotation velocity at the surface of the jet shown in Fig. 10. The Doppler measurement we used did not have the spatial resolution to confirm this and a new Thomson scattering diagnostic with better spatial resolution will be used to look for any enhanced rotation on the edge of the jet.

[1] R. P. Drake, Physics of Plasmas **16**, 055501 (2009).
[2] D. D. Ryutov, B. A. Remington, H. F. Robey, and R. P. Drake, Physics of Plasmas **8**, 1804 (2001).
[3] D. D. Ryutov, M. S. Derzon, and M. K. Matzen, Reviews of Modern Physics **72**, 167 (2000).
[4] D. J. Ampleford, S. V. Lebedev, S. N. Bland, S. C. Bott, J. P. Chittenden, C. A. Jennings, V. L. Kantsyrev, A. S. Safronova, V. V. Ivanov, D. A. Fedin, P. J. Laca, M. F. Yilmaz, V. Nalajala, I. Shrestha, K. Williamson, G. Osborne, A. Haboub, and A. Ciardi, Physics of Plasmas **14**, 102704 (2007).
[5] S. V. Lebedev, A. Ciardi, D. J. Ampleford, S. N. Bland, S. C. Bott, J. P. Chittenden, G. N. Hall, J. Rapley, C. A. Jennings, A. Frank, E. G. Blackman, and T. Lery, Monthly Notices of the Royal Astronomical Society **361**, 97 (2005).
[6] E. Falize, S. Bouquet, and C. Michaut, Journal of Physics: Conference Series **112**, 042016 (2008).
[7] E. Falize, C. Michaut, and S. Bouquet, The Astrophysical Journal **730**, 96 (2011).
[8] C. D. Gregory, J. Howe, B. Loupias, S. Myers, M. M. Notley, Y. Sakawa, A. Oya, R. Kodama, M. Koenig, and N. C. Woolsey, The Astrophysical Journal **676**, 420 (2008).
[9] V. T. Tikhonchuk, P. Nicola, X. Ribeyre, C. Stenz, G. Schurtz, A. Kasperczuk, T. Pisarczyk, L. Juha, E. Krousky, K. Masek, M. Pfeifer, K. Rohlena, J. Skala, J. Ullschmied, M. Kalal, D. Klir, J. Kravarik, P. Kubes, and P. Pisarczyk, Plasma Physics and Controlled Fusion **50**, 124056 (2008).

[10] D. D. Ryutov, N. L. Kugland, H. S. Park, C. Plechaty, B. A. Remington, and J. S. Ross, Plasma Physics and Controlled Fusion **54**, 105021 (2012).

[11] C. E. Seyler and M. R. Martin, Physics of Plasmas **18**, 012703 (2011).

[12] P.-A. Gourdain, I. C. Blesener, J. B. Greenly, D. A. Hammer, P. F. Knapp, B. R. Kusse, and P. C. Schrafel, Physics of Plasmas **17**, 012706 (2010).

[13] P.-A. Gourdain, J. Greenly, D. Hammer, P. F. Knapp, B. R. Kusse, S. Pikuz, P. Schrafel, and T. Shelkovenko, IEEE Transactions on Plasma Science **38**, 3363 (2010).

[14] P.-A. Gourdain, I. C. Blesener, J. B. Greenly, D. A. Hammer, P. F. Knapp, B. R. Kusse, S. A. Pikuz, and T. C. Shelkovenko, Plasma Physics and Controlled Fusion **52**, 055015 (2010).

[15] P.-A. Gourdain, J. B. Greenly, D. A. Hammer, B. R. Kusse, S. A. Pikuz, C. E. Seyler, T. C. Shelkovenko, and P. F. Knapp, Physics of Plasmas **19**, 022701 (2012).

[16] P.-A. Gourdain and C. E. Seyler, Physical Review Letters **110**, 015002 (2013).

[17] F. Suzuki-Vidal, S. V. Lebedev, A. Ciardi, S. N. Bland, J. P. Chittenden, G. N. Hall, A. Harvey-Thompson, A. Marocchino, C. Ning, C. Stehle, A. Frank, E. G. Blackman, S. C. Bott, and T. Ray, Astrophysics and Space Science **322**, 19 (2009).

[18] F. Suzuki-Vidal, S. V. Lebedev, S. N. Bland, G. N. Hall, G. Swadling, A. J. Harvey-Thompson, J. P. Chittenden, A. Marocchino, A. Ciardi, A. Frank, E. G. Blackman, and S. C. Bott, Physics of Plasmas **17**, 112708 (2010).

[19] F. Suzuki-Vidal, S. V. Lebedev, M. Krishnan, J. Skidmore, G. F. Swadling, M. Bocchi, A. J. Harvey-Thompson, S. Patankar, G. C. Burdiak, P. de Grouchy, L. Pickworth, S. J. P. Stafford, L. Suttle, M. Bennett, S. N. Bland, J. P. Chittenden, G. N. Hall, E. Khoory, R. A. Smith, A. Ciardi, A. Frank, R. E. Madden, K. Wilson-Elliot, and P. Coleman, High Energy Density Physics **9**, 141 (2013).

[20] F. Suzuki-Vidal, S. Lebedev, S. Bland, G. Hall, A. Harvey-Thompson, J. Chittenden, A. Marocchino, S. Bott, J. Palmer, and A. Ciardi, IEEE Transactions on Plasma Science **38**, 581 (2010).

[21] J. B. Greenly, J. D. Douglas, D. A. Hammer, B. R. Kusse, S. C. Glidden, and H. D. Sanders, Review of Scientific Instruments **79**, 073501 (2008).

[22] S. A. Pikuz, V. M. Romanova, N. V. Baryshnikov, M. Hu, B. R. Kusse, D. B. Sinars, T. A. Shelkovenko, and D. A. Hammer, Review of Scientific Instruments **72**, 1098 (2001).

[23] K. J. Peterson, D. B. Sinars, E. P. Yu, M. C. Herrmann, M. E. Cuneo, S. A. Slutz, I. C. Smith, B. W. Atherton, M. D. Knudson, and C. Nakhleh, Physics of Plasmas **19**, 092701 (2012).

[24] P. C. Schrafel, P. A. Gourdain, J. B. Greenly, and B. R. Kusse, in *The 39th IEEE International Conference on Plasma Science* (2012).

[25] P. D. Desai, H. M. James, and C. Y. Ho, Journal of Physical and Chemical Reference Data **13**, 1131 (1984).

[26] M. Martin, *Generalized Ohm'S Law At The Plasma-Vacuum Interface*, Ph.D. thesis (2010), 2015-08-05.